

## Manipulation of the photonic spin Hall effect in a cavity magnomechanical system

Muqaddar Abbas <sup>1</sup>, Ghaisud Din,<sup>1</sup> Hamid R. Hamed <sup>2,\*</sup> and Pei Zhang<sup>1,†</sup>

<sup>1</sup>Ministry of Education Key Laboratory for Nonequilibrium Synthesis and Modulation of Condensed Matter, Shaanxi Province Key Laboratory of Quantum Information and Quantum Optoelectronic Devices, School of Physics, Xi'an Jiaotong University, Xi'an, Shaanxi 710049, China

<sup>2</sup>Institute of Theoretical Physics and Astronomy, Vilnius University, Sauletekio 3, Vilnius LT-10257, Lithuania



(Received 28 November 2024; accepted 30 April 2025; published 15 May 2025)

In this paper, we examine the theoretical implications of photonic spin Hall effect (PSHE) amplification in a cavity magnomechanics system. In the framework of the PSHE, we show that spin-orbit interactions cause separation of space across the transverse plane between photons with opposing spins. Our findings reveal that the formation of photonic spin can be tuned across both positive and negative values, depending on the Brewster angle, while varying the magnon-phonon coupling. Notably, we find that in the absence of magnon-phonon coupling, we have magnomechanically induced transparency window at resonance and the PSHE has a higher peak value. Further in the presence of magnon-phonon coupling, the absorption peak occurs at resonance, which leads to a decrease of the PSHE. However, we observe a significant enhancement of the PSHE at two distinct detuning points where light transmission is maximized. Additionally, probe field detuning emerges as a crucial factor in controlling the PSHE. These results suggest that dynamically tuning the coupling between cavity magnons and magnon-phonon modes can greatly enhance the PSHE, presenting new opportunities for advanced nanoscale light manipulation.

DOI: [10.1103/PhysRevA.111.053716](https://doi.org/10.1103/PhysRevA.111.053716)

### I. INTRODUCTION

The photonic spin Hall effect (PSHE) refers to the spin-dependent transverse displacement of light that occurs perpendicular to the plane of incidence [1]. It originates from the coupling between the spin along with orbital angular momenta of light, causing different polarization states to undergo distinct shifts upon reflection or refraction, resulting in a fascinating interplay between spin and spatial displacement [2]. As a result, beams with distinct polarizations can be spatially separated, depending on the spin state of the photons [3]. This effect is sometimes referred to as the Imbert-Fedorov effect. It demonstrates how different polarization states can result in distinct lateral displacements when light interacts with an interface [4].

Spin-dependent splitting has captivated researchers' interest ever since the pioneering Stern-Gerlach experiment proved electron spin quantization. This experiment gave early evidence for the quantized nature of angular momentum and particles associated with spin [5]. The PSHE closely resembles the spin Hall effect observed in condensed-matter physics [6], as it manifests as the splitting of right circularly polarized (RCP) and left circularly polarized (LCP) light, occurring perpendicular to the plane of incidence when a linearly polarized Gaussian beam [either transverse electric (TE) or transverse magnetic (TM)] interacts with an optical interface. This spin-dependent splitting occurs in both reflected and transmitted light waves, resulting from the differential phase

accumulation in the RCP and LCP components of these waves [2]. This phase, arising from light-matter interactions, is known as the Berry phase and it exhibits equal magnitudes but opposite signs for RCP and LCP light. Since phase plays a crucial role in determining the magnitude and direction of light propagation, the opposing Berry phases of RCP and LCP light lead to their spatial separation at the optical interface. In essence, the PSHE introduces additional spin degrees of freedom for the versatile manipulation of light. This capability shows great promise in applications such as quantum information processing and plasmonics [2,7], spin-based nanophotonic devices [8], optical sensing [9], and precise metrology [10].

To broaden the scope of these applications, achieving a pronounced PSHE is essential. However, the effect is often weak, resulting in transverse shifts at the nanometer scale due to limited spin-orbit interaction. Consequently, enhancing and controlling the PSHE presents a significant challenge, which is crucial for advancing modern photonics. Overcoming this hurdle is vital for the development of more efficient and effective photonic devices that leverage the unique properties of spin-dependent phenomena. Recently, a significant PSHE, as well as high performance for any incident polarized light, was obtained by employing complete internal as well as external reflection [11], along with anisotropy impedance of the inconsistencies within the microwave spectrum [12]. Investigations employing quantum weak measurements [13] demonstrated that the PSHE exhibits pronounced enhancement in the vicinity of the Brewster angle upon reflection.

Another captivating phenomenon gaining attention is the cavity magnomechanics (CMM) that explores the interactions between magnons (collective spin excitations in magnetic

\*Contact author: hamid.hamed@tfai.vu.lt

†Contact author: zhangpei@mail.ustc.edu.cn

materials), photons confined in electromagnetic cavities, and mechanical vibrations (phonons). These interactions, typically studied in hybrid quantum systems within a cavity, have significant implications for the performance of the system [14,15]. Systems focused on collective spin excitations, known as magnons, in magnetic materials like yttrium iron garnet (YIG) have garnered substantial attention and achieved notable advancements in recent years [16–19]. A key advantage of magnonic systems is their exceptional ability to coherently interact with various quantum systems, including microwave photons [20–23], optical photons [24], and superconducting qubits [25]. These interactions have given rise to systems such as magnon-qubit hybrids, magnomechanics, cavity optomagnonics [26], magnomechanical frequency combs [27], and cavity magnonics ring spectroscopy [28]. Strong coupling between microwave cavity photons and magnons in YIG crystals, which was theoretically predicted, has also been successfully demonstrated in experiments [29]. This achievement is especially significant as it has catalyzed research in the rapidly growing field of CMM. The YIG-based magnonic system offers additional advantages, such as wide frequency tunability and low dissipation rates, which have further accelerated progress in this area. Recently, researchers have investigated the manipulation of the Goos-Hänchen shift in the reflected portion of an incident probe field within a CMM system using the stationary phase method [30].

Despite significant research on the PSHE, its behavior within a CMM system remains largely unexplored, which is the central focus of this study. This work aims to fill that gap by demonstrating how such a system offers enhanced flexibility in manipulating spin-orbit interactions. To control the PSHE in the reflected probe light, we employ a CMM system as a key mechanism in our analysis. Our results suggest that tuning the coupling strength between cavity magnons and magnon-phonon modes can substantially enhance the PSHE, offering promising prospects for nanoscale light manipulation. Investigating the PSHE in CMM systems could lead to advancements in spin-based applications such as optical sensing. This framework not only deepens our understanding of these systems but also reveals possibilities for harnessing their unique properties in various technological domains.

Although the fundamental principles of the PSHE are well understood, incorporating it into a CMM system introduces a new dimension of tunability through magnon-phonon interactions. The PSHE has gained considerable attention for its ability to govern spin-dependent photon dynamics in various optical platforms, including plasmonic structures [31], photonic crystals [32], and atomic systems [33–35]. However, the investigation of the PSHE within a CMM system, where external magnetic fields and mechanical vibrations provide dynamic control, remains largely unexplored. This work addresses this gap by demonstrating how such a system enhances the flexibility of spin-orbit interaction manipulation, offering unprecedented control over light-matter interactions.

Following our exploration of the proposed framework in this study, we now focus on applying the necessary mathematical formulations to derive expressions for the output field. Section II provides a detailed overview of our model system along with the corresponding equations to determine the effective susceptibility of the intracavity magnonics system. In

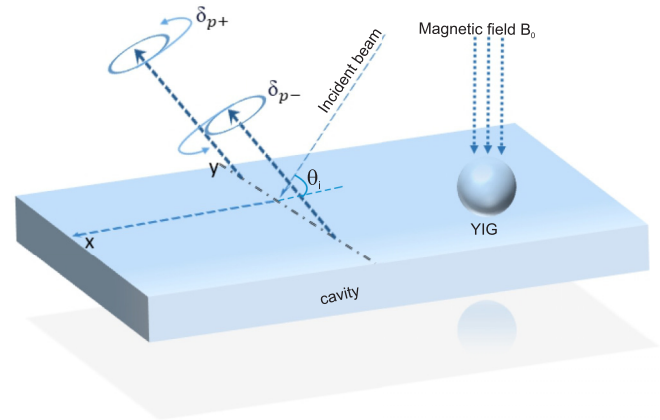


FIG. 1. The system under discussion is modeled through the placement of the YIG sphere that lies within a single cavity. At an angle  $\theta_i$ , a weak probe field having frequency  $\omega_p$  is applied to the cavity. A significant external magnetic field is speculated to drive the YIG sphere, causing magnon-phonon coupling. The direction of the applied magnetic field is shown by the arrows on the YIG sphere.

Sec. III we focus on the calculation of the PSHE, followed by an in-depth analysis of the results in Sec. IV, where we explore both the single and double PSHE. Section V presents a detailed discussion of the PSHE within the framework of CMM. Section VI highlights the main conclusions drawn from the study and outlines their potential implications in a broader context.

## II. EFFECTIVE SUSCEPTIBILITY OF THE MAGNOMECHANICAL SYSTEM

Figure 1 illustrates a theoretical model of a cavity containing a YIG sphere, which is influenced by a probing field with frequency  $\omega_p$ . We focus on a CMM system comprising a single-mode cavity with frequency  $\omega_a$ , inside which a YIG sphere is embedded. The frequency  $\omega_a$  is selected based on recent hybrid magnomechanical experiments [14,36], specifically with  $\omega_a = 2\pi \times 7.86$  GHz for the present configuration. The wavelength of the probe light is determined by the resonant frequencies of both the magnon and cavity modes, yielding a probe light wavelength of  $\lambda = 38.2$  mm. A bias magnetic field is applied to the YIG sphere, leading to the generation of quantized spin waves, referred to as magnon modes. These magnon modes interact with the cavity's electromagnetic field through magnetic dipole interactions. Each mirror has a thickness  $d_1$ , while the thickness of the intracavity magnonic medium is  $d_2$ . The nonlinear susceptibility  $\chi$ , which is represented in terms of permittivity as  $\epsilon_2 = 1 + \chi$ , determines the system's response to external fields. The quadrature of the output field determines the permittivity of the intracavity medium  $\chi$ , while the permittivity of the mirrors is taken as  $\epsilon_1 = 2.22$ , which corresponds to fused silica, a commonly used material in optical cavity setups. Controllable absorption and dispersion are therefore made possible by the alteration of the probe field's resonance conditions. As a result, the probe field's reflection properties are very sensitive to the magnomechanical interactions within the cavity.

The excited magnon modes cause the material's magnetization to shift, which in turn causes magnetostriction to deform the YIG lattice structure. These distortions alter the physical properties of the YIG material, leading to a coupling between phonons and magnons within the YIG sphere. This interaction, known as magnon-phonon coupling, is represented by the parameter  $g_{mb}$ .

The dynamics of this whole system is determined by a mathematical framework, which may be expressed directly as

$$\begin{aligned} H = & \hbar\Delta_c c^\dagger c + \hbar\Delta_m m^\dagger m + \hbar\omega_b b^\dagger b + \hbar g_{mc}(m^\dagger c + mc^\dagger) \\ & + \hbar g_{mb} m^\dagger m(b + b^\dagger) + i\Omega_d(m^\dagger - m) \\ & + i\hbar\mathcal{E}_p(c^\dagger e^{-i\delta t} - e^{i\delta t}c), \end{aligned} \quad (1)$$

where  $\Delta_c = \omega_c - \omega_d$  is the cavity detuning and  $c^\dagger$  and  $c$  represent the creation and annihilation operators, respectively, for the cavity mode. The term  $\hbar\Delta_c c^\dagger c$  corresponds to the free energy of the cavity. Here  $\Delta_m = \omega_m - \omega_d$  is the magnon detuning and  $m^\dagger$  and  $m$  represent the creation and annihilation operators, respectively, for the magnon mode. The term  $\hbar\Delta_m m^\dagger m$  describes the free energy of the magnon modes. The  $\omega_b$  is the frequency of the phonon mode and  $b^\dagger$  and  $b$  represent the creation and annihilation operators, respectively, for the phonon mode. The term  $\hbar\omega_b b^\dagger b$  corresponds to the free energy of the phonon modes. The term  $\hbar g_{mc}(m^\dagger c + mc^\dagger)$  describes the interaction between the magnon and cavity modes, where  $g_{mc}$  represents the coupling strength between the magnons and the cavity photons. Similarly, the term  $\hbar g_{mb} m^\dagger m(b + b^\dagger)$  represents the magnon-phonon interaction, with  $g_{mb}$  denoting the coupling strength between magnons and phonons.

As discussed earlier, the YIG sphere is subjected to an external magnetic field, which is represented by the term  $i\Omega_d(m^\dagger - m)$ . Here  $\Omega_d = \frac{\sqrt{5}}{4}\gamma\sqrt{\rho V}B_0$  describes the coupling strength of the driving field, where  $B_0$  is the amplitude of the magnetic field,  $\omega_d$  is its frequency,  $\rho$  is the spin density, and  $V$  is the volume of the YIG sphere. Additionally, a probe laser field with amplitude  $\mathcal{E}_p$  and frequency  $\omega_p$  is applied to the cavity, as illustrated in Fig. 1. The amplitude of the probe light field is specified as  $\mathcal{E}_p = \sqrt{\frac{2\kappa_a P_p}{\hbar\omega_p}}$ . Here  $P_p$  is the power of the probe field,  $\kappa_a$  is the cavity photon decay rate, and  $\delta = \omega_p - \omega_d$ .

In our analysis, we will solve the Hamiltonian and derive the quantum Langevin equations using the Heisenberg operator approach. This method allows us to thoroughly analyze the system's evolution and gain insight into its dynamical behavior. The temporal evolution of the operators in quantum Langevin dynamics, incorporating both the Hamiltonian and dissipation effects described by a Lindblad operator  $\mathcal{L}$ , is governed by the equation [37]

$$\frac{d\mathcal{O}}{dt} = -\frac{i}{\hbar}[\mathcal{O}, H] + D[\mathcal{L}]\mathcal{O} + \mathcal{N}, \quad (2)$$

where  $\mathcal{N}$  accounts for external noise sources, such as vacuum fluctuations and thermal noise. The Lindblad dissipator is defined as

$$D[\mathcal{L}]\mathcal{O} = \mathcal{L}^\dagger \mathcal{O} \mathcal{L} - \frac{1}{2}(\mathcal{L}^\dagger \mathcal{L} \mathcal{O} + \mathcal{O} \mathcal{L}^\dagger \mathcal{L}). \quad (3)$$

For a cavity mode with photon annihilation operator  $c$ , the decay is described by the Lindblad operator

$$\mathcal{L} = \sqrt{2\kappa_a}c, \quad (4)$$

where  $\kappa_a$  is the cavity decay rate. Employing Eq. (4) in Eq. (3) yields

$$D[\mathcal{L}]\mathcal{O} = 2\kappa_a c^\dagger \mathcal{O} c - \kappa_a (c^\dagger c \mathcal{O} + \mathcal{O} c^\dagger c). \quad (5)$$

If  $\mathcal{O}$  corresponds to the field operator  $c$ , this expression reduces to a standard decay term

$$\frac{dc}{dt} = -\frac{i}{\hbar}[c, H] - \kappa_a c + \mathcal{N}. \quad (6)$$

The expression  $\mathcal{O}$  in Eq. (2) denotes the operators ( $c, m, b$ ) in the Hamiltonian, and  $\mathcal{N}$  includes contributions from both input vacuum noise and the Brownian noise operator. Using Eqs. (1) and (2), we derive the Heisenberg-Langevin equations. The coupled dynamical equations, obtained from the total Hamiltonian in Eq. (1), account for both dissipative processes and quantum fluctuation effects and are expressed as

$$\dot{c} = -(i\Delta_c + \kappa_a)c - ig_{mc}m + \mathcal{E}_p e^{-i\delta t} + \sqrt{2\kappa_a}c_{\text{in}}, \quad (7)$$

$$\begin{aligned} \dot{m} = & -(i\Delta_m + \kappa_m)m - ig_{mc}c - ig_{mb}m(b + b^\dagger) + \Omega_d \\ & + \sqrt{2\kappa_a}m_{\text{in}}, \end{aligned} \quad (8)$$

$$\dot{b} = -(i\omega_b + \kappa_b)b - ig_{mb}m^\dagger m + \zeta, \quad (9)$$

where  $\kappa_m$  and  $\kappa_b$  are the decay rates for the magnon mode and the phonon modes, and  $c_{\text{in}}$ ,  $m_{\text{in}}$ , and  $\zeta$  are the quantum noise operators associated with the cavity mode, magnon mode, and mechanical modes, respectively. It is important to note that the mean values of the quantum noise, Brownian noise, and input operator are equal to zero [38].

The first-order fluctuations are linearized as  $c = c_s + \delta c$ ,  $m = m_s + \delta m$ , and  $b = b_s + \delta b$  [39]. By substituting these first-order fluctuations into Eqs. (7)–(9) and setting the time derivatives to zero, the steady-state mean values for the cavity mode  $c_s$ , the magnon mode  $m_s$ , and phonon modes  $b_s$  are obtained as

$$\begin{aligned} c_s = & \frac{-ig_{mc}m_s}{i\Delta_c + \kappa_a}, \\ m_s = & \frac{-ig_{mc}c_s + \Omega_d}{i\Delta'_m + \kappa_m}, \\ b_s = & \frac{-ig_{mb}|m_s|^2}{i\omega_b + \kappa_b}, \end{aligned} \quad (10)$$

where  $\Delta'_m = \Delta_m + g_{mb}(b_s + b_s^\dagger)$ . The equations of motion for the quantum fluctuations are nonlinear and are expressed as

$$\delta\dot{c} = -(\kappa_a + i\Delta_c)\delta c - ig_{mc}\delta m + \mathcal{E}_p e^{-i\delta t}, \quad (11)$$

$$\begin{aligned} \delta\dot{m} = & -(i\Delta_m + \kappa_m)\delta m - ig_{mc}\delta c - ig_{mb}(\delta b + \delta b^\dagger)\delta m + \Omega_d, \end{aligned} \quad (12)$$

$$\delta\dot{b} = -(i\omega_b + \kappa_b)\delta b - ig_{mb}\delta m^\dagger \delta m. \quad (13)$$

The nonlinear terms in these equations, such as  $-ig_{mb}(\delta b + \delta b^\dagger)\delta m$  and  $-ig_{mb}\delta m^\dagger \delta m$ , arise from the interactions among

the cavity, magnon, and phonon modes and are crucial for capturing the system's nonlinear dynamics. To analyze the equations of motion (11)–(13), we solve them perturbatively using the ansatz  $\delta\mathcal{O} = \sum_{n \in \{-, +\}} \mathcal{O}_n e^{in\delta t}$ , where  $\mathcal{O} = \{c, m, b\}$  [39]. The oscillation in the cavity is primarily attributed to magnomechanical effects induced by applying the driving field in our proposed model. Furthermore, the amplitude and phase modulations within the system can be finely tuned through the interplay of the control and probe

laser fields. These modulations give rise to both Stokes and anti-Stokes sideband dispersion in the control beam. The first-order expression for the transmitted probe field  $c_-$  is subsequently derived using the aforementioned methodology and is given by

$$c_- = \frac{\mathcal{B}}{\mathcal{A}}, \quad (14)$$

where

$$\mathcal{B} = \mathcal{E}_p (g_{mc}^2 \alpha_3 \alpha_5 \alpha_6 + \alpha_2 \alpha_3 \alpha_4 \alpha_5 \alpha_6 - G_{mb}^2 g_{mc}^2 \alpha_5 + G_{mb}^2 \alpha_2 \alpha_3 \alpha_5 - G_{mb}^2 \alpha_2 \alpha_4 \alpha_5 + G_{mb}^2 g_{mc}^2 \alpha_6 - G_{mb}^2 \alpha_2 \alpha_3 \alpha_6 + G_{mb}^2 \alpha_2 \alpha_4 \alpha_6), \quad (15)$$

$$\begin{aligned} \mathcal{A} = & g_{mc}^4 \alpha_5 \alpha_6 + g_{mc}^2 \alpha_1 \alpha_3 \alpha_5 \alpha_6 + g_{mc}^2 \alpha_2 \alpha_4 \alpha_5 \alpha_6 + \alpha_1 \alpha_2 \alpha_3 \alpha_4 \alpha_5 \alpha_6 - G_{mb}^2 g_{mc}^2 \alpha_1 \alpha_5 + G_{mb}^2 g_{mc}^2 \alpha_2 \alpha_5 + G_{mb}^2 \alpha_1 \alpha_2 \alpha_3 \alpha_5 \\ & - G_{mb}^2 \alpha_1 \alpha_2 \alpha_4 \alpha_5 + G_{mb}^2 g_{mc}^2 \alpha_1 \alpha_6 - G_{mb}^2 g_{mc}^2 \alpha_2 \alpha_6 - G_{mb}^2 \alpha_1 \alpha_2 \alpha_3 \alpha_6 + G_{mb}^2 \alpha_1 \alpha_2 \alpha_4 \alpha_6, \end{aligned} \quad (16)$$

and

$$\alpha_1 = -i\delta + i\Delta_c + \kappa_a, \quad (17)$$

$$\alpha_2 = -i\delta - i\Delta_c + \kappa_a, \quad (18)$$

$$\alpha_3 = -i\delta + i\Delta_m + \kappa_m, \quad (19)$$

$$\alpha_4 = -i\delta - i\Delta_m + \kappa_m, \quad (20)$$

$$\alpha_5 = -i\delta + i\omega_b + \kappa_b, \quad (21)$$

$$\alpha_6 = -i\delta - i\omega_b + \kappa_b. \quad (22)$$

Here the effective magnomechanical coefficient of coupling is given by  $G_{mb} = g_{mb} m_s$ , which can be adjusted using an external magnetic field while keeping  $g_{mb}$  constant. We examine the output probe field (OPF) spectrum by using the input-output relation given in [40]. To make things simpler, this relationship might be stated as

$$E_{\text{out}} + \mathcal{E}_p e^{-i\delta t} = \sqrt{2\kappa_a} c, \quad (23)$$

where

$$E_{\text{out}} = E_{\text{out}}^0 + E_{\text{out}}^+ \mathcal{E}_p e^{-i\delta t} + E_{\text{out}}^- \mathcal{E}_p e^{i\delta t}. \quad (24)$$

By solving Eqs. (23) and (24), we get the expressions

$$E_{\text{out}}^+ = \frac{\sqrt{2\kappa_a} c_-}{\mathcal{E}_p} - 1 \quad (25)$$

and

$$E_{\text{out}}^+ + 1 = \frac{\sqrt{2\kappa_a} c_-}{\mathcal{E}_p} = E_T. \quad (26)$$

One way to conceptualize the OPF is as the effective susceptibility of the intracavity medium  $\chi = E_T$ , which is represented by Eq. (26). The complex variable  $\chi$ , which has both imaginary and real components, defines the quadrature for the field  $E_T$  [40–42]. It is possible to measure this quadrature using homodyne detection techniques in addition to the formula  $\chi = \chi_r + i\chi_i$ . The real component  $\chi_r$  represents the absorption spectrum, while the imaginary portion  $\chi_i$  represents the dispersion spectrum of the probing field. So we

find the permittivity of intracavity medium by the relation  $\epsilon_2 = 1 + \chi$ .

### III. CALCULATION OF THE PSHE

Figure 1 shows the cavity mirror  $M_1$  illuminated by a TM-polarized light beam along with a TE-polarized light beam coming from the vacuum at an angle of incidence  $\theta_i$ . While the monochromatic Gaussian beam may penetrate the layered structure or be reflected at the interface, our primary focus is on the reflected part, particularly under conditions where the angle of incidence and polarization significantly influence the reflection behavior. Upon reflection, the RCP and LCP components of the incident beam experience a spatial separation along the direction perpendicular to the plane of incidence, i.e., along the  $y$  axis, as depicted in Fig. 1. The PSHE is a polarization-dependent optical phenomenon that develops when photons with opposing helicities are separated by light spin-orbit coupling. The complex reflection coefficients for TM polarization ( $R_p$ ) and TE polarization ( $R_s$ ) for the three-layer structure can be computed using the transfer-matrix approach. The transfer matrix for the  $j$ th layer of a given configuration is expressed as [43,44]

$$N_j(k_z, \omega_p, d_j) = \begin{pmatrix} \cos(k_x^j) & \frac{i \sin(k_x^j)}{q_j} \\ iq_j \sin(k_x^j) & \cos(k_x^j) \end{pmatrix}. \quad (27)$$

Here  $k_x^j = d_j \sqrt{\epsilon_j k^2 - k^2 \sin^2(\theta_i)}$  is the  $x$  component of the wave vector in the  $j$ th layer of the medium. Similarly, the thickness of the  $j$ th layer is given by  $d_j$ , where  $j$  is the number of the corresponding layer of the medium and  $q_j = \sqrt{\epsilon_k k^2 - k^2 \sin^2(\theta_i)}$ . In this context,  $\epsilon_k$  is the permittivity of the  $k$ th layer. Further  $k = 2\pi/\lambda$  is the wave vector and  $\lambda$  is the wavelength of light. In our case, we have three layers: 1 and 3 are the cavity walls with permittivity  $\epsilon_1$  and  $\epsilon_3$ , and 2 is the intracavity medium that consists of a YIG sphere with permittivity  $\epsilon_2 = 1 + \chi$ . The total transfer matrix for the incident and reflected probe light beam for our proposed model can be written as [43,45,46]

$$x(k_z, \omega_p) = N_1(k_z, \omega_p, d_1) N_2(k_z, \omega_p, d_2) N_3(k_z, \omega_p, d_3). \quad (28)$$

The coefficient of reflection also depends on the intracavity permittivity  $\epsilon_2$ , which may be successfully regulated by adjusting  $\chi$ , as shown by Eq. (28). Following a number of computations along with mathematical derivations, the probing field's TE-polarized reflection coefficient may be expressed as

$$R_s = \frac{q_{1s}(x_{11} + x_{12}q_{3s}) - (q_{3s}^2 x_{22} + x_{21})}{q_{1s}(x_{11} + x_{12}q_{3s}) + (q_{3s}^2 x_{22} + x_{21})}, \quad (29)$$

where  $x_{ij}$  are the elements of the transfer matrix  $x(k_z, \omega_p)$ ,  $q_{1s} = \sqrt{\epsilon_1 k^2 - k^2 \sin^2(\theta_i)}$ , and  $q_{3s} = \sqrt{\epsilon_3 k^2 - k^2 \sin^2(\theta_i)}$ .

Likewise, by substituting  $p_{jp}$  for  $q_{js}$ , we can determine the probe field's TM-polarized coefficient of reflection as

$$R_p = \frac{p_{1p}(x_{11} + x_{12}p_{3p}) - (p_{3p}^2 x_{22} + x_{21})}{p_{1p}(x_{11} + x_{12}p_{3p}) + (p_{3p}^2 x_{22} + x_{21})}, \quad (30)$$

where  $p_{1p} = \frac{\sqrt{\epsilon_1 k^2 - k^2 \sin^2(\theta_i)}}{\epsilon_1}$  and  $p_{3p} = \frac{\sqrt{\epsilon_3 k^2 - k^2 \sin^2(\theta_i)}}{\epsilon_3}$ . The field amplitudes of two circular parts that comprise the reflected light are set up within the reflection system for a TM-polarized Gaussian beam incident on the interface, as given by [47]

$$\begin{aligned} E_r^\pm(x_r, y_r, z_r) &= \frac{\omega_0}{\omega} \exp\left(-\frac{x_r^2 + y_r^2}{\omega}\right) \\ &\times \left(R_p - \frac{2ix_r}{k\omega} \frac{\partial R_p}{\partial \theta} \mp \frac{2y_r \cot(\theta)}{k\omega} (R_s + R_p)\right). \end{aligned} \quad (31)$$

Here the radius of the beam  $\omega$  is defined as  $\omega = \omega_0 [1 + (\frac{2z_r}{k_1 \omega_0})^2]^{1/2}$ , where  $\omega_0$  denotes the radius of the waist of the incident beam and  $z_r = \frac{k_1 \omega_0^2}{2}$  corresponds to the Rayleigh length. The  $(x_r, y_r, z_r)$  display the arrangement of coordinates for light that is reflected, accompanied by the superscript  $\pm$  denoting the distinct spin configurations. The aforementioned transverse displacement for light that is reflected may be articulated as

$$\delta_p^\pm = \frac{\int y_r |E_r^\pm(x_r, y_r, z_r)|^2 dx_r dy_r}{\int |E_r^\pm(x_r, y_r, z_r)|^2 dx_r dy_r}. \quad (32)$$

From Eqs. (31) and (32), the corresponding transverse spin-displacement components  $\delta_p^+$  and  $\delta_p^-$  in terms of the three-layer cavity-magnon system's refractive coefficients can be expressed as [44,48]

$$\delta_p^\pm = \mp \frac{k_1 \omega_0^2 \text{Re}(1 + \frac{R_s}{R_p}) \cot \theta_i}{k_1^2 \omega_0^2 + \left|\frac{\partial \ln R_p}{\partial \theta_i}\right|^2 + \left|(1 + \frac{R_s}{R_p}) \cot \theta_i\right|^2}. \quad (33)$$

The transverse displacement  $\delta_p^\pm$  corresponds to the shift experienced by the (left and right) circularly polarized components of the incoming beam, measured perpendicular to the plane of incidence. Here the wave vector in the incident medium is given by  $k_1 = \sqrt{\epsilon_1} k$ , where  $\epsilon_1$  is the relative permittivity. In the following analysis, we concentrate on the shift associated with the RCP,  $\delta_p^+$ . Due to the inherent spin symmetry of circular polarization, the LCP component undergoes an equivalent shift in magnitude but in the opposite direction. As a result, it

TABLE I. Experimental parameters [14,36].

Parameter	Symbol	Value
cavity-magnon coupling strength	$g_{mc}$	$2\pi \times 2$ MHz
magnon-phonon coupling strength	$G_{mb}$	$2\pi \times 0.1$ MHz
mechanical frequency	$\omega_b$	$2\pi \times 15$ MHz
cavity dissipation rate	$\kappa_a$	$2\pi \times 2.1$ MHz
magnon dissipation rate	$\kappa_m$	$2\pi \times 0.1$ MHz
phonon dissipation rate	$\kappa_b$	$2\pi \times 150$ Hz
temperature	$T$	10 mK
power	$P$	10 mW

suffices to examine a single polarization state to fully capture the nature of the transverse displacement.

#### IV. RESULTS

We provide the results of our numerical simulations in this section. We use the parameters from recent hybrid magnomechanical system experiments [14,36] for these computations, which are also provided in Table I. Specifically, we use  $\omega_b = 2\pi \times 15$  MHz,  $\kappa_b = 2\pi \times 150$  Hz,  $\kappa_m = 2\pi \times 0.1$  MHz,  $\kappa_a = 2\pi \times 2.1$  MHz, and the magnon-cavity-photon coupling  $g_{mc} = 2\pi \times 2$  MHz. To investigate the PSHE, we consider  $\epsilon_0 = 1$ ,  $\epsilon_1 = 2.22$ ,  $\epsilon_2 = 1 + \chi$ ,  $\epsilon_3 = 2.22$ ,  $d_1 = 4$  mm, and  $d_2 = 45$  mm [30]. The system includes a YIG sphere with a diameter  $D = 250$   $\mu\text{m}$ , spin density  $\rho = 4.22 \times 10^{27} \text{ m}^{-3}$ , and gyromagnetic ratio  $\gamma = 2\pi \times 28$  GHz/T [14,36]. For the chosen parameters, the driving magnetic field is set to  $B_0 \leq 0.5$  mT (corresponding to  $G_{mb}/2\pi \leq 1.5$  MHz) to ensure that the system operates within the stable regime [49].

To examine the results discussed in this paper, we start by analyzing Fig. 2. Using Eq. (26), we plotted the real part of the output probe field as a function of the normalized detuning  $\delta/\omega_b$ . In the first scenario, we set the coupling parameter for the magnon-phonon interaction to zero ( $G_{mb} = 0$ ). Under this condition, the spectrum of the output probe field reveals a phenomenon known as magnon-induced transparency (MIT). This effect signifies that light is transmitted through the cavity without any contribution from magnon-phonon coupling. The appearance of MIT in the spectrum, which reflects the interference between the probe field and the cavity mode, is illustrated in Fig. 2(a).

Equation (33) reveals that the transverse displacement  $\delta_p^\pm$  is governed by the behavior of the reflection coefficients corresponding to both TE- and TM-polarized components of the incident beam. To better understand this dependence, we begin by analyzing the angular response of the reflection coefficients as a function of the incident angle of the incoming beam. Figure 2(b) presents the magnitudes of the reflection coefficients for the TE polarization ( $R_s$ ) and the TM polarization ( $R_p$ ), demonstrating their dependence on the angle of incidence. This analysis provides a foundation for understanding the role of polarization in influencing the transverse shift.

For the TE-polarized wave ( $R_s$ ), represented by the purple solid curve, the reflection coefficient shows a strong dependence on the angle of incidence as shown in Fig. 2(b). At small angles, the reflection coefficient is relatively low, indicating

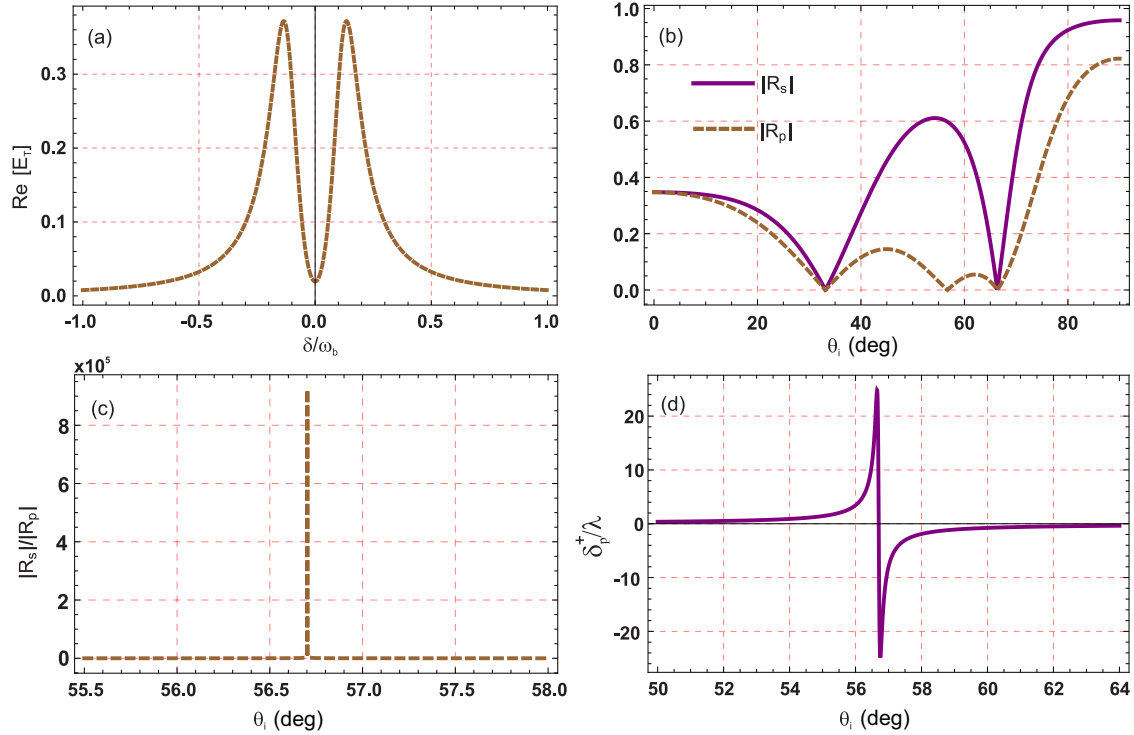


FIG. 2. (a) Absorption profile of the transmitted probe field, represented by  $\text{Re}(E_T)$  [with  $E_T$  defined in Eq. (26)], plotted versus the normalized probe detuning  $\delta/\omega_b$  in the absence of magnon-phonon coupling, i.e.,  $G_{mb} = 0$  (brown dashed curve). The parameters are mechanical frequency  $\omega_b = 2\pi \times 15$  MHz, mechanical damping  $\kappa_b = 2\pi \times 150$  Hz, magnon decay rate  $\kappa_m = 2\pi \times 0.1$  MHz, cavity decay rate  $\kappa_a = 2\pi \times 2.1$  MHz, and magnon-photon coupling strength  $g_{mc} = 2\pi \times 2$  MHz. (b) Fresnel reflection coefficients  $|R_s|$  and  $|R_p|$  depicted as a function of the angle of incidence  $\theta_i$  for TE and TM polarization, respectively. (c) Ratio  $|R_s|/|R_p|$  as a function of  $\theta_i$ , revealing its enhancement near the Brewster angle. (d) The PSHE, quantified by the normalized transverse shift  $\delta_p^+/\lambda$  [given by Eq. (33)], plotted against the angle of incidence  $\theta_i$ . The shift changes sign near the Brewster angle where the reflection coefficient ratio  $|R_s|/|R_p|$  attains its peak value. In (b)–(d) the detuning is fixed at  $\delta/\omega_b = 0$ . The remaining parameters are wavelength  $\lambda = 38.2$  mm, permittivities  $\epsilon_0 = 1$  and  $\epsilon_1 = \epsilon_3 = 2.22$ , layer thicknesses  $d_1 = 4$  mm and  $d_2 = 45$  mm, and beam waist  $\omega_0 = 50\lambda$ .

increased transmission and reduced reflection. As the angle increases,  $R_s$  initially decreases and reaches a minimum value near  $33^\circ$ . This behavior can be explained by the fact that at smaller angles, the electric field of the TE wave is more parallel to the interface, resulting in weaker interactions with the surface and consequently lower reflection.

After reaching this minimum,  $R_s$  increases rapidly and reaches a peak near the Brewster angle, approximately  $56.7^\circ$ . This rise occurs because, with increasing angle, the electric field becomes more perpendicular to the interface, enhancing its interaction with the surface and leading to stronger reflection. Beyond this peak,  $R_s$  decreases again, reaching another minimum around  $67^\circ$ , which can be attributed to the onset of destructive interference effects and the angular dependence of the reflection coefficient, which causes the reflected amplitude to decrease due to phase mismatch between the incident and reflected waves. At higher angles, approaching  $90^\circ$ ,  $R_s$  increases once more, tending to a value close to 1, indicating near-total reflection. This is because at high angles the incident wave is nearly perpendicular to the surface, resulting in maximum interaction and reflection [see Fig. 2(b)].

For a TM-polarized wave ( $R_p$ ), depicted by the brown dashed curve, the reflection coefficient also depends on the angle of incidence as shown in Fig. 2(b). Notably, at normal incidence ( $\theta = 0^\circ$ ), the reflection coefficients for both

polarizations are equal, indicating that the initial reflection behavior is identical for both TE and TM waves. As the incident angle increases,  $R_p$  decreases, reaching a minimum around  $33^\circ$ , similar to the TE-polarized waves. This decrease arises due to the redistribution of the electromagnetic field at oblique incidence; specifically, the magnetic-field component of the TM wave becomes more aligned with the interface, reducing its effective interaction with the boundary. Consequently, less energy is reflected and the reflection coefficient decreases.

As the angle of incidence continues to rise,  $R_p$  exhibits a modest increase before undergoing a rapid decline, ultimately vanishing at the Brewster angle ( $\theta_B \approx 56.7^\circ$ ). This minimum indicates complete transmission with no reflection, a characteristic feature of TM-polarized light at the Brewster angle, where the reflected and refracted rays become orthogonal, resulting in the cancellation of the reflected component. Beyond this point,  $R_p$  increases again, peaking around  $60^\circ$ , but the increase is less pronounced compared to  $R_s$ . After this peak,  $R_p$  decreases again, reaching a minimum near  $67^\circ$ , similar to the behavior of  $R_s$ . At higher incident angles,  $R_p$  increases once more, but the increase is less steep than that of  $R_s$ , and the reflection remains lower than that of TE-polarized waves [see Fig. 2(b)].

As illustrated in Fig. 2(b), the reflection coefficients for both TE and TM polarizations exhibit a dependence on the

angle of incidence. This dependence is critical in determining the ratio  $|R_s/R_p|$ , which in turn governs the transverse shift. Equation (33) indicates that the normalized transverse displacement  $\delta_p^+/\lambda$  is modulated by the ratio between the reflection coefficients of the TE- and TM-polarized components, represented by  $R_s$  and  $R_p$ , respectively, for a given angle of incidence. Notably, when the magnitude of this ratio exceeds unity, an enhanced transverse shift is observed. To elucidate this dependence, the angular variation of the ratio  $|R_s/R_p|$  is examined, with the detuning parameter fixed at  $\delta/\omega_b = 0$ , as illustrated in Fig. 2(c). This condition corresponds to the transparency regime, where the maximum contrast in reflection behavior between the two polarization modes is expected. The ratio reaches its maximum value at  $\delta/\omega_b = 0$ , which corresponds to the transparency window. Further, the ratio increases sharply near the Brewster angle ( $\theta_B \approx 56.7^\circ$ ), due to the contrasting ways in which TE- and TM-polarized light interact with the interface at this specific angle. At the Brewster angle, the TM-polarized reflection coefficient  $R_p$  vanishes, as depicted by the brown dashed curve in Fig. 2(b). This develops because, at this particular angle, the reflected TM wave is negated owing to destructive interference generated by boundary conditions at the contact. The TE-polarized reflection coefficient  $R_s$  does not reach zero at the Brewster angle; instead, it remains nonzero. This disparity ensures that  $R_s$  dominates the ratio near the Brewster angle, further amplifying  $|R_s/R_p|$ . Thus, near the Brewster angle, the interaction of light with the interface creates conditions in which TM-polarized light refracts fully into the second medium, leaving no reflection. However, the TE-polarized light does not follow this behavior and continues to reflect. As a result, the contrast between  $R_s$  and  $R_p$  becomes pronounced, significantly enhancing their ratio. In order to accurately characterize the dynamics near this pivotal angle, the analysis focuses on a narrow range of incident angles  $\theta_i$ .

To elucidate the characteristics of the transverse displacement induced by the PSHE, we next concentrate our analysis on the normalized shift  $\delta_p^+/\lambda$ , which pertains to the RCP component of the reflected beam. In Fig. 2(d) the PSHE  $\delta_p^+/\lambda$  is analyzed versus incident angle  $\theta_i$  at  $\delta/\omega_b = 0$ . To ensure clarity and allow for direct comparison, all parameters are kept constant, highlighting the enhancement of the PSHE at  $\delta/\omega_b = 0$ . The transverse PSHE is observed to be positive for incident angles  $\theta_i < 56.7^\circ$  and becomes negative for  $\theta_i > 56.7^\circ$ . The interference effects that contribute to the transverse shift are controlled by the  $\pi$  shift in phase associated with the Fresnel coefficients  $R_s$  along with  $R_p$ , which causes this sign reversal.

The enhancement of the PSHE at resonance, specifically at  $\delta/\omega_b = 0$ , is primarily driven by two factors. First, at this frequency, magnon-induced transparency significantly reduces absorption, thereby allowing for stronger light-matter interactions that reinforce the spin-dependent splitting. The reduction in absorption minimizes the loss of coherence between the spin components, enabling a more pronounced spin-orbit coupling effect. Second, the phase difference between the TE- and TM-polarized reflection coefficients becomes more pronounced near the Brewster angle, leading to enhanced

constructive interference, which amplifies the transverse spatial shift of the polarization components. Together, these effects result in a significant enhancement of the PSHE at resonance, where the system's transparency and the phase relationship between the polarizations optimize the spin Hall shift.

As we proceed with our study, we introduce the magnon-phonon coupling with a strength of  $G_{mb} = 0.1 \times 2\pi$  MHz, as shown in Fig. 3(a). Upon examining the output probe field spectrum, we observe the emergence of an additional narrow peak within the transparency window at  $\delta/\omega_b = 0$ , represented by the brown dashed curve in Fig. 3(a). This results in the splitting of the single transparency window into two distinct windows, revealing a new aspect of the system's behavior and emphasizing the interaction between magnons and phonons within the cavity [50–52].

Figure 3(b) illustrates the PSHE shift  $\delta_p^+/\lambda$  as a function of the incidence angle  $\theta_i$  at the resonant probe field detuning  $\delta/\omega_b = 0$ , with a fixed incident angle of  $\theta_i = 56.7^\circ$ . A noticeable reduction in the amplitude of the PSHE peaks is observed, which corresponds to the absorption peak at resonance shown in Fig. 3(a). This reduction is primarily attributed to enhanced absorption at resonance, induced by magnon-phonon coupling. As the coupling strength increases, additional absorption channels emerge, modifying the system's spectral response, particularly narrowing the transparency window. This redistribution of optical energy among different modes limits the spectral range available for interaction with the incident light, thereby weakening the spin-dependent splitting. Consequently, the system's ability to maintain coherence and phase integrity of spin-dependent light components diminishes, leading to a suppressed PSHE.

Figure 3(c) presents the PSHE shift  $\delta_p^+/\lambda$  under the same conditions but at an off-resonant probe field detuning of  $\delta/\omega_b = \pm 0.0067$ . Here an enhancement in the amplitude of the PSHE peaks is observed, corresponding to the transparency window at this detuning, as shown in Fig. 3(a). This increase results from the magnon-phonon coupling shifting the transparency window to an off-resonant detuning. In this regime, the redistribution of optical energy broadens the spectral range over which the system effectively interacts with incident light, enhancing the PSHE. The increased transparency at off-resonant detuning improves the system's ability to preserve coherence and phase relationships of spin-dependent components, thereby strengthening the observed PSHE amplitude.

Next we investigate the combined effect of probe field detuning  $\delta/\omega_b$  and incident angle  $\theta_i$  on the PSHE shift. In Fig. 4(a) we display the PSHE shift  $\delta_p^+$  as a function of both the incident angle  $\theta_i$  and probe field detuning  $\delta/\omega_b$ , assuming no magnon-phonon coupling ( $G_{mb}/2\pi = 0$ ). A maximum PSHE of  $24\lambda$  is observed at  $\Delta_p = 0$ . In Fig. 4(b) we present a density plot of the PSHE when the magnon-phonon coupling strength is nonzero ( $G_{mb}/2\pi = 0.1$  MHz). With the coupling turned on, the PSHE increases at two distinct probe field detuning values, as shown in Fig. 4(b). This is due to the splitting of the single magnon-induced transparency into two symmetric transparency windows at equal and opposite detunings of the probe field  $\delta/\omega_b$ . Furthermore, the  $\pi$  shift in phase through

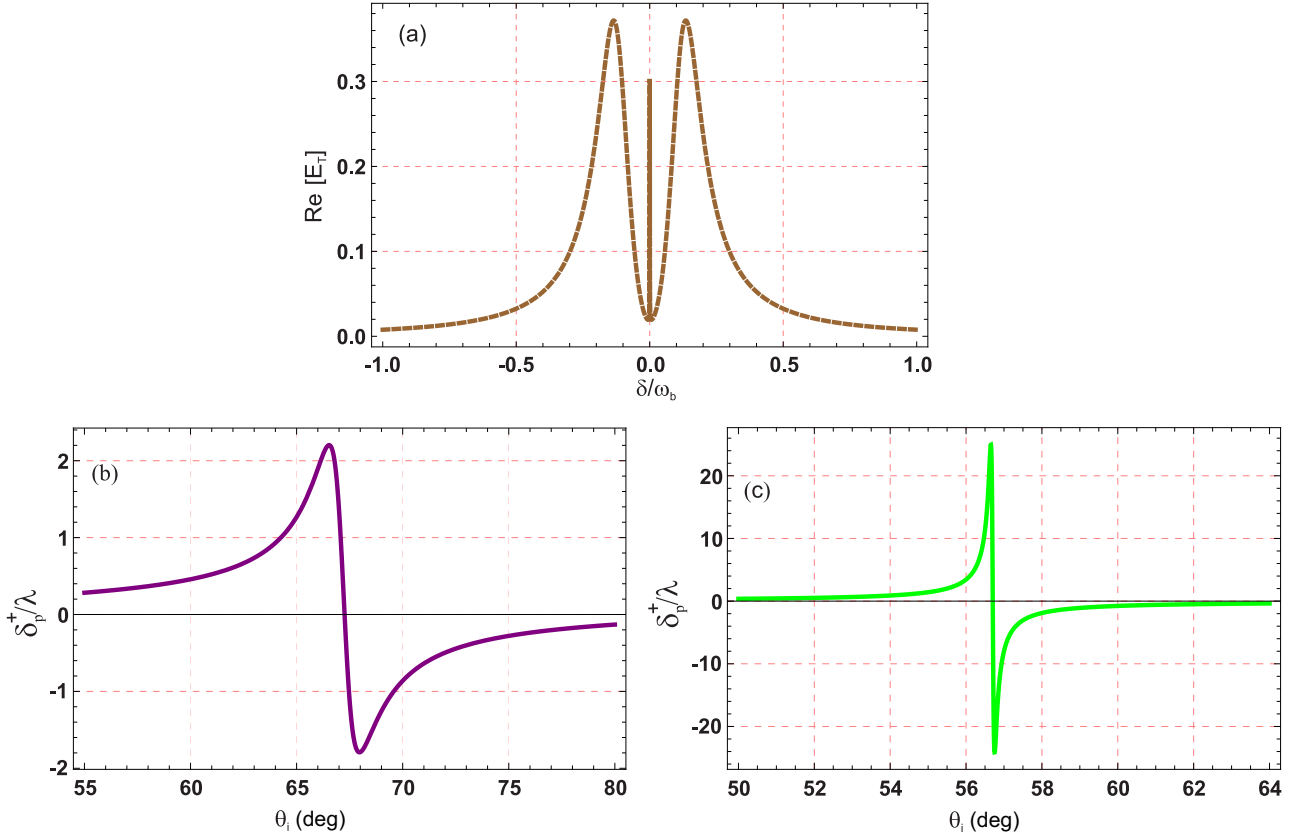


FIG. 3. (a) Absorption characteristics of the output probe field, represented by the real part of  $\text{Re}(E_T)$  [where  $E_T$  is given in Eq. (26)], as a function of the probe field detuning  $\delta/\omega_b$  when the magnon-phonon coupling is active with  $G_{mb} = 2\pi \times 0.1$  MHz. The system parameters are set as follows:  $\omega_b = 2\pi \times 15$  MHz,  $\kappa_b = 2\pi \times 150$  Hz,  $\kappa_m = 2\pi \times 0.1$  MHz,  $\kappa_a = 2\pi \times 2.1$  MHz, and the magnon-cavity-photon coupling strength  $g_{mc} = 2\pi \times 2$  MHz. The PSHE, represented by the normalized transverse shift  $\delta_p^+/\lambda$  for RCP components [as given in Eq. (33)], is plotted against the angle of incident  $\theta_i$  for (b) resonant detuning  $\delta/\omega_b = 0$  and (c) off-resonant detuning  $\delta/\omega_b = \pm 0.0067$ . The other parameters are  $\lambda = 38.2$  mm,  $\epsilon_0 = 1$ ,  $\epsilon_1 = 2.22$ ,  $\epsilon_2 = 1 + \chi$ ,  $\epsilon_3 = 2.22$ ,  $d_1 = 4$  mm,  $d_2 = 45$  mm, and beam waist  $\omega_0 = 50\lambda$ .

the phases of the Fresnel coefficients  $R_s$ , along with  $R_p$  is also responsible for the transverse PSHE's sign change, becoming positive for  $\theta_i < 56.7^\circ$  and negative when  $\theta_i > 56.7^\circ$ .

The observed behavior can be explained by the interplay between the magnon-phonon coupling and the system's resonance properties. When the magnon-phonon coupling is

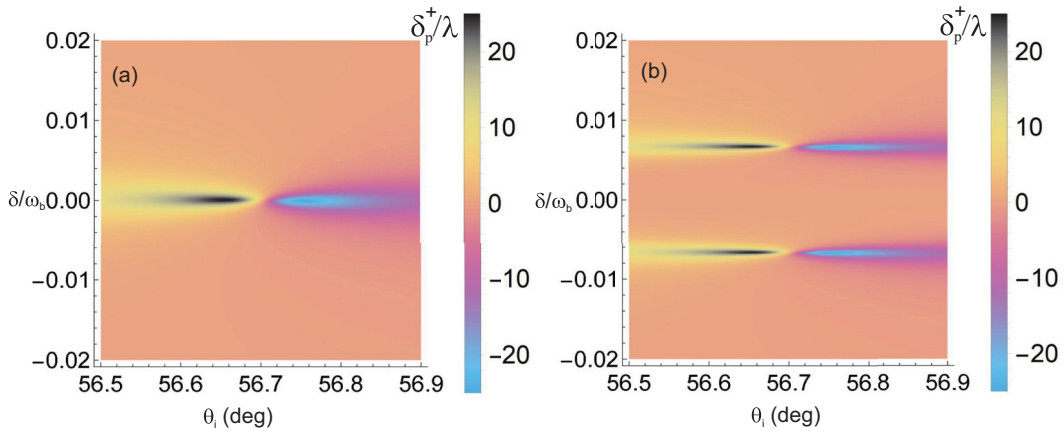


FIG. 4. Density plot of the PSHE  $\delta_p^+/\lambda$  [transverse shift for RCP components given in Eq. (33)] against detuning of the probe field  $\delta/\omega_b$ , along with incident angle  $\theta_i$  when (a) magnon-phonon coupling is off, i.e.,  $G_{mb} = 0$ , and (b) magnon-phonon coupling is on, i.e.,  $G_{mb} = 0.1 \times 2\pi$  MHz. The other parameters are  $\omega_b = 2\pi \times 15$  MHz,  $\kappa_b = 2\pi \times 150$  Hz,  $\kappa_m = 2\pi \times 0.1$  MHz,  $\kappa_a = 2\pi \times 2.1$  MHz, magnon-cavity-photon coupling  $g_{mc} = 2\pi \times 2$  MHz,  $\lambda = 38.2$  mm,  $\epsilon_0 = 1$ ,  $\epsilon_1 = 2.22$ ,  $\epsilon_2 = 1 + \chi$ ,  $\epsilon_3 = 2.22$ ,  $d_1 = 4$  mm,  $d_2 = 45$  mm, and beam waist  $\omega_0 = 50\lambda$ .

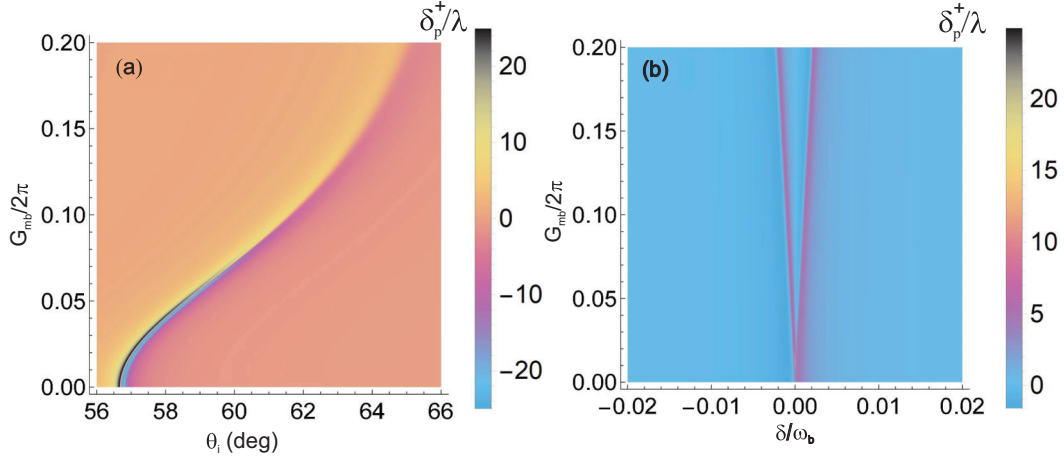


FIG. 5. (a) Density plot of the transverse shift  $\delta_p^+/\lambda$  [transverse shift for RCP components given in Eq. (33)] versus incident angle  $\theta_i$  and magnon-phonon coupling  $G_{mb}$  by considering  $\delta/\omega_b = 0$ . (b) Density plot of the transverse shift  $\delta_p^+/\lambda$  [transverse shift for RCP components given in Eq. (33)] versus detuning  $\delta/\omega_b$  and magnon-phonon coupling  $G_{mb}$  by considering  $\theta_i = 56.7^\circ$ . The other parameters are  $\omega_b = 2\pi \times 15$  MHz,  $\lambda = 38.2$  mm,  $\kappa_b = 2\pi \times 150$  Hz,  $\kappa_m = 2\pi \times 0.1$  MHz,  $\kappa_a = 2\pi \times 2.1$  MHz, magnon-cavity-photon coupling  $g_{mc} = 2\pi \times 2$  MHz,  $\epsilon_0 = 1$ ,  $\epsilon_1 = 2.22$ ,  $\epsilon_2 = 1 + \chi$ ,  $\epsilon_3 = 2.22$ ,  $d_1 = 4$  mm,  $d_2 = 45$  mm, and beam waist  $\omega_0 = 50\lambda$ .

turned on, it splits the single MIT into two symmetric MIT windows at equal and opposite detunings of the probe field. This splitting is due to the interaction between magnons and phonons within the cavity, which introduces additional absorption channels and modifies the spectral response of the system. As a result, the PSHE is enhanced at these two detuning values, reflecting the new transparency windows where light experiences minimal absorption and maximized interaction with the system. The change in the sign of the transverse PSHE around the Brewster angle ( $\theta_i = 56.7^\circ$ ) results from the phase difference that exists among Fresnel reflection coefficients  $R_s$  (TE polarized) and  $R_p$  (TM polarized). This phase shift alters the nature of the interaction between the incident light and the surface, leading to a positive PSHE for angles smaller than the Brewster angle and a negative PSHE for angles larger than it.

To better understand the effect of the quantum parameter, namely, the magnon-phonon coupling strength  $G_{mb}$ , we analyze its influence in conjunction with the incident angle  $\theta_i$  on the PSHE shift at resonance detuning  $\delta/\omega_b = 0$ , as depicted in Fig. 5(a). Initially, when the magnon-phonon coupling is weak, the PSHE is maximized at resonance near the Brewster angle due to minimal absorption. However, as the magnon-phonon coupling strength increases, the PSHE shifts away from the Brewster angle owing to increased absorption at resonance.

Figure 5(b) presents a density graph of the PSHE versus detuning of probe field  $\delta/\omega_b$  and  $G_{mb}/2\pi$ , with  $\theta_i = 56.7^\circ$  remaining constant. In the absence of magnon-phonon coupling, the PSHE exhibits a peak at resonance due to strong spin-orbit interactions of light, where different (left and right) circular polarization components experience distinct spatial shifts. These shifts arise from the inherent coupling between the polarization state and the Berry phase effects. However, as the coupling strength  $G_{mb}$  increases, absorption at resonance becomes more significant, leading to a suppression of the PSHE.

Despite this suppression, two symmetric MIT windows emerge, where absorption is minimized, allowing for an enhancement of the PSHE. As shown in Fig. 5(b), the PSHE is significantly enhanced at two distinct detuning points where light transmission is maximized.

This observed behavior stems from the intricate interplay between magnon-phonon coupling and the system's resonance properties. Initially, weak coupling enhances the PSHE near the Brewster angle due to minimal absorption, preserving the coherence of the spin-orbit interaction. However, stronger coupling introduces additional absorption channels, suppressing the PSHE and shifting it away from the Brewster angle. This coupling also modifies the spectral response, splitting the transparency window into two symmetric MIT regions where the polarization-dependent phase shift is restored. Consequently, the PSHE is maximized at detunings corresponding to these MIT windows, where light-matter interactions are optimized, and the spin-dependent splitting is reinforced.

## V. DISCUSSION

From the above analysis, we establish a direct connection between MIT and the PSHE, leading to an enhanced, tunable, and split displacement effect that sets our work apart from previous research. While the physics of the medium appears to enter the PSHE through a single complex parameter, the permittivity  $\epsilon_2 = 1 + \chi$ , this effective susceptibility  $\chi$  is not fixed. Instead, it is actively modulated by magnon-phonon coupling  $G_{mb}$  and external magnetic fields, enabling dynamic control over the PSHE within our model. This tunability surpasses the capabilities of conventional optical systems, as the system's dispersion properties can be precisely manipulated by adjusting parameters such as  $G_{mb}$  and external magnetic fields. These modifications allow for controlled, real-time adjustments of spin-dependent beam displacements, offering new degrees of freedom to manipulate spin-orbit effects in photonic systems.

Unlike previous studies of the PSHE in atomic systems, which typically rely on cavity QED techniques [33–35], our approach utilizes the transfer-matrix method. This method is more suitable for magnomechanical systems, where experimental configurations differ from those in traditional cavity QED setups. The ability to dynamically tune the PSHE without relying on optical pumping or high-power lasers, a common limitation in atomic platforms, makes this approach particularly advantageous for on-chip photonic devices requiring reconfigurability. This reconfigurability, combined with the introduction of new physical degrees of freedom, opens new pathways for tunable photonic devices and quantum information processing.

The phenomenon of MIT has been discussed in more detail in the literature [50–52]. Our work does not treat MIT as a mere phenomenon but as a mechanism for actively controlling the PSHE, a connection that has not been explored previously. By demonstrating how MIT splitting influences spin-dependent beam displacements, we establish a direct link between magnomechanics and spin-orbit photonics, enabling functionalities like magnetic-field-driven PSHE sign reversal and dual amplification windows. The mechanical mode ( $\omega_b = 2\pi \times 15$  MHz) introduces a low-frequency mechanical degree of freedom, which is absent in atomic systems. Mechanical vibrations can dynamically shift the MIT window, enabling strain- or temperature-tunable spin Hall shifts, capabilities that are unattainable in atomic media.

This platform also offers a theoretical framework for the development of hybrid quantum technologies. By integrating the PSHE with a tunable magnomechanical system, we open up new possibilities for strain-mediated spin-orbit devices and magnetic-field-reconfigurable photonics. For instance, mechanical vibrations at  $\omega_b = 2\pi \times 15$  MHz could modulate PSHE shifts via strain coupling, enabling phonon-driven photonic circuits. Additionally, adjusting  $G_{mb}$  via  $B_0$  allows for dynamic control of spin-dependent beam displacements, which could be used for on-chip signal routing. These concepts are uniquely feasible in solid-state systems like ours,

which are compatible with cryogenic operation. The low decay rate of the mechanical mode ( $\kappa_b = 2\pi \times 150$  Hz) ensures stable PSHE operation even at 10 mK, aligning with the noise resilience requirements of future quantum hardware.

While experimental validation is still needed, our results lay the groundwork for advancing spin-orbit photonics in hybrid quantum platforms, offering new avenues for tunable photonic devices and quantum information processing.

## VI. CONCLUSION

In conclusion, the PSHE in a hybrid CMM system exhibits unique features that are strongly influenced by the system’s spectrum characteristics and the coupling between the magnon and phonon. In the absence of coupling, the PSHE is significantly enhanced at resonance due to MIT, which reduces absorption and allows for stronger spin-orbit interactions. However, the inclusion of magnon-phonon coupling opens additional absorption channels, resulting in modified spectral responses and splitting the transparency window into two separate regions. The increased absorption suppresses the PSHE at resonance but enhances it at off-resonant detuning, indicating a change in the system’s interaction with the probe light. These findings highlight the intricate dynamics between light-matter interactions, spin-orbit coupling, and the system’s structural features, suggesting promising opportunities for quantum sensing and communication technologies.

## ACKNOWLEDGMENTS

The authors would like to express their sincere gratitude to Muhammad Waseem for his invaluable discussions, insightful comments, and contributions to the development of this work. His expertise and constructive feedback greatly enhanced the quality of the paper. This work was supported by the National Natural Science Foundation of China (Grant No. 12174301), the Natural Science Basic Research Program of Shaanxi (Program No. 2023-JC-JQ-01), and the Fundamental Research Funds for the Central Universities.

- 
- [1] M. Onoda, S. Murakami, and N. Nagaosa, *Phys. Rev. Lett.* **93**, 083901 (2004).
  - [2] K. Y. Bliokh, F. J. Rodríguez-Fortuño, F. Nori, and A. V. Zayats, *Nat. Photonics* **9**, 796 (2015).
  - [3] K. Y. Bliokh and Y. P. Bliokh, *Phys. Rev. Lett.* **96**, 073903 (2006).
  - [4] C. Imbert, *Phys. Rev. D* **5**, 787 (1972).
  - [5] D. E. Platt, *Am. J. Phys.* **60**, 306 (1992).
  - [6] J. E. Hirsch, *Phys. Rev. Lett.* **83**, 1834 (1999).
  - [7] K. Y. Bliokh, D. Smirnova, and F. Nori, *Science* **348**, 1448 (2015).
  - [8] N. Shitrit, I. Yulevich, E. Maguid, D. Ozeri, D. Veksler, V. Kleiner, and E. Hasman, *Science* **340**, 724 (2013).
  - [9] L. Xie, X. Qiu, L. Luo, X. Liu, Z. Li, Z. Zhang, J. Du, and D. Wang, *Appl. Phys. Lett.* **111**, 191106 (2017).
  - [10] X. Zhou, X. Ling, H. Luo, and S. Wen, *Appl. Phys. Lett.* **101**, 251602 (2012).
  - [11] M. Kim, D. Lee, T. H.-Y. Nguyen, H.-J. Lee, G. Byun, and J. Rho, *ACS Photonics* **8**, 2705 (2021).
  - [12] M. Kim, D. Lee, H. Cho, B. Min, and J. Rho, *Laser Photonics Rev.* **15**, 2000393 (2021).
  - [13] M. Kim, D. Lee, Y. Kim, and J. Rho, *Nanophotonics* **11**, 4591 (2022).
  - [14] X. Zhang, C. Zou, L. Jiang, and H. Tang, *Sci. Adv.* **2**, e1501286 (2016).
  - [15] X. Zuo, Z.-Y. Fan, H. Qian, M.-S. Ding, H. Tan, H. Xiong, and J. Li, *New J. Phys.* **26**, 031201 (2024).
  - [16] D. Lachance-Quirion, Y. Tabuchi, A. Gloppe, K. Usami, and Y. Nakamura, *Appl. Phys. Express* **12**, 070101 (2019).
  - [17] H. Yuan, Y. Cao, A. Kamra, R. A. Duine, and P. Yan, *Phys. Rep.* **965**, 1 (2022).
  - [18] B. Zare Rameshti, S. Viola Kusminskiy, J. A. Haigh, K. Usami, D. Lachance-Quirion, Y. Nakamura, C.-M. Hu, H. X. Tang, G. E. Bauer, and Y. M. Blanter, *Phys. Rep.* **979**, 1 (2022).

- [19] X. Zhang, *Mater. Today Electron.* **5**, 100044 (2023).
- [20] H. Huebl, C. W. Zollitsch, J. Lotze, F. Hocke, M. Greifenstein, A. Marx, R. Gross, and S. T. B. Goennenwein, *Phys. Rev. Lett.* **111**, 127003 (2013).
- [21] Y. Tabuchi, S. Ishino, T. Ishikawa, R. Yamazaki, K. Usami, and Y. Nakamura, *Phys. Rev. Lett.* **113**, 083603 (2014).
- [22] X. Zhang, C.-L. Zou, L. Jiang, and H. X. Tang, *Phys. Rev. Lett.* **113**, 156401 (2014).
- [23] M. Goryachev, W. G. Farr, D. L. Creedon, Y. Fan, M. Kostylev, and M. E. Tobar, *Phys. Rev. Appl.* **2**, 054002 (2014).
- [24] A. Osada, R. Hisatomi, A. Noguchi, Y. Tabuchi, R. Yamazaki, K. Usami, M. Sadgrove, R. Yalla, M. Nomura, and Y. Nakamura, *Phys. Rev. Lett.* **116**, 223601 (2016).
- [25] D. Xu, X.-K. Gu, H.-K. Li, Y.-C. Weng, Y.-P. Wang, J. Li, H. Wang, S.-Y. Zhu, and J. Q. You, *Phys. Rev. Lett.* **130**, 193603 (2023).
- [26] Z. Shen, G.-T. Xu, M. Zhang, Y.-L. Zhang, Y. Wang, C.-Z. Chai, C.-L. Zou, G.-C. Guo, and C.-H. Dong, *Phys. Rev. Lett.* **129**, 243601 (2022).
- [27] G.-T. Xu, M. Zhang, Y. Wang, Z. Shen, G.-C. Guo, and C.-H. Dong, *Phys. Rev. Lett.* **131**, 243601 (2023).
- [28] G.-T. Xu, M. Zhang, Z.-Y. Wang, Y. Wang, Y.-X. Liu, Z. Shen, G.-C. Guo, and C.-H. Dong, *Fund. Res.* **3**, 45 (2023).
- [29] O. O. Soykal and M. E. Flatté, *Phys. Rev. Lett.* **104**, 077202 (2010).
- [30] M. Waseem, M. Irfan, and S. Qamar, *Phys. Rev. A* **110**, 033711 (2024).
- [31] X. Yu, X. Wang, Z. Li, L. Zhao, F. Zhou, J. Qu, and J. Song, *Nanophotonics* **10**, 3031 (2021).
- [32] B. Xie, G. Su, H.-F. Wang, F. Liu, L. Hu, S.-Y. Yu, P. Zhan, M.-H. Lu, Z. Wang, and Y.-F. Chen, *Nat. Commun.* **11**, 3768 (2020).
- [33] R.-G. Wan and M. S. Zubairy, *Phys. Rev. A* **101**, 033837 (2020).
- [34] J. Wu, J. Zhang, S. Zhu, and G. S. Agarwal, *Opt. Lett.* **45**, 149 (2020).
- [35] M. Waseem, M. Shah, and G. Xianlong, *Phys. Rev. A* **110**, 033104 (2024).
- [36] X. Li, W.-X. Yang, T. Shui, L. Li, X. Wang, and Z. Wu, *J. Appl. Phys.* **128**, 191101 (2020).
- [37] S. Huang and G. S. Agarwal, *Phys. Rev. A* **83**, 023823 (2011).
- [38] K. Qu and G. S. Agarwal, *Phys. Rev. A* **87**, 031802(R) (2013).
- [39] R. W. Boyd, *Nonlinear Optics* (Academic, New York, 2010).
- [40] G. S. Agarwal and S. Huang, *Phys. Rev. A* **81**, 041803(R) (2010).
- [41] A. Hafeez, Ziauddin, M. Abbas, and S. Qamar, *J. Opt. Soc. Am. B* **36**, 3070 (2019).
- [42] S. Weis, R. Rivière, S. Deléglise, E. Gavartin, O. Arcizet, A. Schliesser, and T. J. Kippenberg, *Science* **330**, 1520 (2010).
- [43] M. Born and E. Wolf, *Principles of Optics* (Elsevier, Amsterdam, 1999).
- [44] L. Wu, H.-S. Chu, W. S. Koh, and E.-P. Li, *Opt. Express* **18**, 14395 (2010).
- [45] L.-G. Wang, M. Ikram, and M. S. Zubairy, *Phys. Rev. A* **77**, 023811 (2008).
- [46] Ziauddin, S. Qamar, and M. S. Zubairy, *Phys. Rev. A* **81**, 023821 (2010).
- [47] X.-J. Tan and X.-S. Zhu, *Opt. Lett.* **41**, 2478 (2016).
- [48] Y. Xiang, X. Jiang, Q. You, J. Guo, and X. Dai, *Photonics Res.* **5**, 467 (2017).
- [49] T.-X. Lu, H. Zhang, Q. Zhang, and H. Jing, *Phys. Rev. A* **103**, 063708 (2021).
- [50] A. Munir, M. Abbas, Ziauddin, W.-M. Liu, and P. Zhang, *J. Opt. Soc. Am. B* **40**, 1756 (2023).
- [51] Q. Liao, K. Peng, and H. Qiu, *Chin. Phys. B* **32**, 054205 (2023).
- [52] K. Mukherjee and P. C. Jana, *Eur. Phys. J. Plus* **138**, 1127 (2023).